



# The Lowest of the Low: Discovery of SN 2019gsc and the Nature of Faint Iax Supernovae

Shubham Srivastav<sup>1</sup>, Stephen J. Smartt<sup>1</sup>, Giorgos Leloudas<sup>2</sup>, Mark E. Huber<sup>3</sup>, Ken Chambers<sup>3</sup>, Daniele B. Malesani<sup>2</sup>, Jens Hjorth<sup>4</sup>, James H. Gillanders<sup>1</sup>, A. Schultz<sup>3</sup>, Stuart A. Sim<sup>1</sup>, Katie Auchettl<sup>4,5,6</sup>, Johan P. U. Fynbo<sup>7,8</sup>, Christa Gall<sup>4</sup>, Owen R. McBrien<sup>1</sup>, Armin Rest<sup>9,10</sup>, Ken W. Smith<sup>1</sup>, Radoslaw Wojtak<sup>4</sup>, and David R. Young<sup>1</sup>

<sup>1</sup> Astrophysics Research Centre, School of Mathematics and Physics, Queen's University Belfast, Belfast BT7 1NN, UK; [s.srivastav@qub.ac.uk](mailto:s.srivastav@qub.ac.uk)

<sup>2</sup> DTU Space, National Space Institute, Technical University of Denmark, DK-2800 Kongens Lyngby, Denmark

<sup>3</sup> Institute of Astronomy, University of Hawaii, 2680 Woodlawn Drive, Honolulu, HI 96822, USA

<sup>4</sup> DARK, Niels Bohr Institute, University of Copenhagen, Lyngbyvej 2, DK-2100 Copenhagen Ø, Denmark

<sup>5</sup> Department of Astronomy and Astrophysics, University of California, Santa Cruz, CA 95064, USA

<sup>6</sup> School of Physics, The University of Melbourne, Parkville, VIC 3010, Australia

<sup>7</sup> The Cosmic Dawn Center (DAWN), Vibenshuset, Lyngbyvej 2, DK-2100 Copenhagen, Denmark

<sup>8</sup> Niels Bohr Institute, University of Copenhagen, Lyngbyvej 2, DK-2100 Copenhagen Ø, Denmark

<sup>9</sup> Space Telescope Science Institute, 3700 San Martin Drive, Baltimore, MD 21218, USA

<sup>10</sup> Department of Physics and Astronomy, Johns Hopkins University, Baltimore, MD 21218, USA

Received 2020 January 24; revised 2020 February 14; accepted 2020 February 15; published 2020 March 31

## Abstract

We present the discovery and optical follow-up of the faintest supernova-like transient known. The event (SN 2019gsc) was discovered in a star-forming host at 53 Mpc by ATLAS. A detailed multicolor light curve was gathered with Pan-STARRS1 and follow-up spectroscopy was obtained with the Nordic Optical Telescope and Gemini-North. The spectra near maximum light show narrow features at low velocities of 3000–4000 km s<sup>-1</sup>, similar to the extremely low-luminosity SNe 2010ae and 2008ha, and the light curve displays a similar fast decline ( $\Delta m_{15}(r) = 0.91 \pm 0.10$  mag). SNe 2010ae and 2008ha have been classified as SNe Iax, and together the three either make up a distinct physical class of their own or are at the extreme low-luminosity end of this diverse supernova population. The bolometric light curve is consistent with a low kinetic energy of explosion ( $E_k \sim 10^{49}$  erg s<sup>-1</sup>), a modest ejected mass ( $M_{ej} \sim 0.2 M_\odot$ ), and radioactive powering by <sup>56</sup>Ni ( $M_{Ni} \sim 2 \times 10^{-3} M_\odot$ ). The spectra are quite well reproduced with radiative transfer models (TARDIS) and a composition dominated by carbon, oxygen, magnesium, silicon, and sulfur. Remarkably, all three of these extreme Iax events are in similar low-metallicity star-forming environments. The combination of the observational constraints for all three may be best explained by deflagrations of near  $M_{Ch}$  hybrid carbon–oxygen–neon white dwarfs that have short evolutionary pathways to formation.

*Unified Astronomy Thesaurus concepts:* [Supernovae \(1668\)](#); [Type Ia supernovae \(1728\)](#)

## 1. Introduction

SNe Ia are widely accepted to be explosions resulting from thermonuclear runaway in degenerate carbon–oxygen (CO) white dwarfs (WDs) in close binary systems (Hoyle & Fowler 1960; Nomoto et al. 1984). They constitute a remarkably homogeneous subclass of explosions that follow the width–luminosity relation (e.g., Phillips 1993; Hamuy et al. 1996), but the precise nature of the progenitor, and the details of the explosion mechanism, remain open questions (Howell 2011; Maoz et al. 2014).

SNe Iax (Foley et al. 2013) are a peculiar subclass of Ia events, named after the prototypical Iax event SN 2002cx (Li et al. 2003). SNe Iax are characterized by low ejecta velocities ( $\sim 2000$ – $8000$  km s<sup>-1</sup>) and typically low luminosities, although they span a wide range in luminosity, from  $M \simeq -14$  for SN 2008ha (Foley et al. 2009; Valenti et al. 2009) to  $M \simeq -19$  for SN 2008A (McCully et al. 2014a). Unlike other thermonuclear events, late-time spectra of SNe Iax do not exhibit a true nebular phase, with permitted lines of (mainly) Fe II persisting well beyond a year past maximum light (Jha 2017, and references therein). While a majority of SNe Iax show a positive correlation between peak luminosity and expansion velocity (McClelland et al. 2010), notable outliers like SN 2009ku (Narayan et al. 2011) and SN 2014ck (Tomasella et al. 2016) are known to exist.

At the extreme faint end of the objects that are broadly classified as SNe Iax are the low-energy explosions SN 2008ha and SN 2010ae (Foley et al. 2009, 2010; Valenti et al. 2009; Stritzinger et al. 2014). With absolute peak magnitudes of  $M_V = -14.2$  and  $-13.8 \gtrsim M_V \gtrsim -15.3$ , respectively, their physical nature has been disputed. A core-collapse scenario has been suggested for SN 2008ha (Valenti et al. 2009). However, this would require these two members of the Iax subclass to be distinct (along with possibly others), whereas the evidence seems to suggest a kinship with the more luminous members of the Iax family (Jha 2017). A progenitor scenario involving a weak deflagration of a white dwarf leaving a bound remnant behind has been proposed (e.g., Jordan et al. 2012; Kromer et al. 2013; Fink et al. 2014) to explain the peculiarities of SNe Iax.

This Letter reports the discovery of SN 2019gsc (ATLAS19mbg) by the ATLAS survey (Tonry et al. 2018), and results of detailed follow-up with Pan-STARRS1, the Nordic Optical Telescope (NOT), and Gemini-North. We note the independent study on SN 2019gsc presented by Tomasella et al. (2002), and briefly compare our results with theirs in Section 5.

## 2. Discovery and Follow-up

SN 2019gsc (ATLAS19mbg) was discovered by ATLAS on 2019 June 02.36 UT (MJD 58636.36) in the cyan filter, at a

**Table 1**  
Summary of Photometric Observations of SN 2019gsc from ZTF and Pan-STARRS1

| MJD      | Phase  | <i>g</i>     | <i>r</i>     | <i>i</i>     | <i>z</i>     | <i>y</i>     | Instrument |
|----------|--------|--------------|--------------|--------------|--------------|--------------|------------|
| 58628.25 | −10.45 | >20.62       | >20.49       | ...          | ...          | ...          | ZTF        |
| 58632.28 | −6.47  | ...          | > 20.44      | ...          | ...          | ...          | ZTF        |
| 58635.23 | −3.55  | 19.85 ± 0.17 | 19.93 ± 0.13 | ...          | ...          | ...          | ZTF        |
| 58638.22 | −0.59  | 19.92 ± 0.18 | 19.72 ± 0.12 | ...          | ...          | ...          | ZTF        |
| 58639.38 | +0.55  | 19.88 ± 0.05 | 19.68 ± 0.04 | 19.80 ± 0.04 | 19.87 ± 0.05 | 19.88 ± 0.19 | PS1        |
| 58641.26 | +2.41  | 19.99 ± 0.09 | 19.63 ± 0.07 | 19.76 ± 0.06 | 19.74 ± 0.07 | 19.74 ± 0.21 | PS1        |
| 58642.26 | +3.40  | 20.06 ± 0.09 | 19.63 ± 0.09 | 19.93 ± 0.12 | 19.82 ± 0.14 | 20.04 ± 0.33 | PS1        |
| 58643.26 | +4.39  | 20.13 ± 0.04 | 19.69 ± 0.03 | 19.72 ± 0.02 | 19.78 ± 0.03 | ...          | PS1        |
| 58644.27 | +5.39  | 20.15 ± 0.06 | 19.70 ± 0.04 | 19.79 ± 0.04 | 19.74 ± 0.04 | 20.26 ± 0.17 | PS1        |
| 58645.41 | +6.52  | 20.46 ± 0.18 | 19.78 ± 0.09 | 19.70 ± 0.07 | 19.69 ± 0.10 | ...          | PS1        |
| 58646.31 | +7.41  | 20.56 ± 0.12 | 19.80 ± 0.04 | 19.80 ± 0.03 | 19.81 ± 0.04 | 20.04 ± 0.12 | PS1        |
| 58647.35 | +8.43  | 20.81 ± 0.13 | 19.93 ± 0.04 | 19.86 ± 0.03 | 19.88 ± 0.04 | 20.13 ± 0.13 | PS1        |
| 58648.36 | +9.43  | 20.74 ± 0.16 | 19.92 ± 0.06 | 19.86 ± 0.04 | 19.83 ± 0.05 | 20.24 ± 0.18 | PS1        |
| 58649.34 | +10.40 | 20.99 ± 0.28 | 19.94 ± 0.08 | 19.93 ± 0.05 | 19.89 ± 0.05 | 20.19 ± 0.16 | PS1        |
| 58650.27 | +11.32 | 21.46 ± 0.24 | 20.15 ± 0.06 | 20.09 ± 0.04 | 20.01 ± 0.04 | 20.11 ± 0.10 | PS1        |
| 58651.30 | +12.34 | 20.91 ± 0.25 | 20.16 ± 0.09 | 20.11 ± 0.07 | 20.04 ± 0.08 | 20.15 ± 0.22 | PS1        |
| 58652.29 | +13.32 | ...          | 20.43 ± 0.23 | 20.26 ± 0.14 | 20.04 ± 0.09 | ...          | PS1        |
| 58656.27 | +17.26 | 21.55 ± 0.25 | 20.58 ± 0.07 | 20.38 ± 0.08 | 20.23 ± 0.14 | 20.29 ± 0.30 | PS1        |
| 58662.28 | +23.20 | 21.64 ± 0.13 | 20.83 ± 0.09 | 20.74 ± 0.09 | 20.45 ± 0.08 | 20.50 ± 0.25 | PS1        |
| 58666.28 | +27.15 | 22.24 ± 0.27 | 21.11 ± 0.07 | 21.01 ± 0.06 | 20.64 ± 0.07 | ...          | PS1        |
| 58670.28 | +31.11 | ...          | 21.60 ± 0.25 | ...          | 20.70 ± 0.11 | ...          | PS1        |
| 58674.28 | +35.06 | ...          | 21.56 ± 0.27 | 21.10 ± 0.15 | 20.79 ± 0.12 | ...          | PS1        |
| 58688.28 | +48.91 | ...          | 22.17 ± 0.20 | 21.95 ± 0.15 | 21.22 ± 0.11 | ...          | PS1        |

**Note.** The phase (in days) is relative to the epoch of *g*-band maximum on MJD 58638.82 in the SN rest frame.

magnitude of  $c = 19.7 \pm 0.2$  (Smartt et al. 2019). ATLAS is a twin 0.5 m telescope system on the islands of Haleakala and Mauna Loa. With a field of view  $\sim 29 \text{ deg}^2$ , each telescope surveys the sky robotically above decl.  $-40^\circ$  with a cadence of 2 days (Tonry et al. 2018). The images are obtained in the two filters, cyan and orange, that are roughly equivalent to SDSS  $g + r$  and  $r + i$ , respectively. Using the *Lasair* broker (Smith et al. 2019), we note a prior detection by the Zwicky Transient Facility (ZTF; Bellm et al. 2019) on 2019 June 01.23 UT (MJD 58635.23), at  $g = 19.85 \pm 0.17$ . The transient was not detected in ZTF images on MJD 58632.28 and 58628.30, to a limiting magnitude of 20.46 and 20.50, respectively, in the ZTF  $r$  filter. The transient was subsequently classified as a type Ia event by Leloudas et al. (2019), who noted similarity of its spectral features with the Ia SN 2010ae. The host galaxy SBS 1436+529A has a redshift of  $z = 0.0113$  or a heliocentric recessional velocity of  $3388 \text{ km s}^{-1}$  (Argudo-Fernández et al. 2015). Correcting the velocity for the effects of Virgo infall, Great Attractor, and Shapley supercluster, we adopt a distance modulus of  $\mu = 33.60 \text{ mag}$  (assuming  $H_0 = 73 \text{ km s}^{-1} \text{ Mpc}^{-1}$ ).

Follow-up photometry (Table 1) was obtained using the 1.8 m Pan-STARRS1 telescope (Chambers et al. 2016) on Haleakala equipped with a 1.4 Gigapixel camera (GPC1,  $0.26 \text{ arcsec pixel}^{-1}$ ). Images were obtained in the *grizy<sub>p1</sub>* filters (Tonry et al. 2012) and processed with the Image Processing Pipeline described in Magnier et al. (2016a). Due to SN 2019gsc being superposed to its host galaxy, image subtraction was essential for all epochs of photometry. The Pan-STARRS1 Science Consortium (Chambers et al. 2016)  $3\pi$  survey data were used as templates, point-spread-function fitting photometry was carried out, and photometric calibration was done against PS1 reference stars in the field (Magnier et al. 2016b; Waters et al. 2016).

**Table 2**  
Log of Spectroscopic Observations for SN 2019gsc

| Date<br>(yyyy mm dd) | MJD      | Phase<br>(days) | Instrument    | Exposure<br>(s) |
|----------------------|----------|-----------------|---------------|-----------------|
| 2019 Jun 3           | 58637.97 | −0.84           | ALFOSC/NOT    | $4 \times 600$  |
| 2019 Jun 6           | 58640.00 | +1.17           | ALFOSC/NOT    | $4 \times 600$  |
| 2019 Jun 8           | 58642.09 | +3.23           | ALFOSC/NOT    | $4 \times 600$  |
| 2019 Jun 12          | 58646.88 | +7.97           | ALFOSC/NOT    | $4 \times 900$  |
| 2019 Jun 20          | 58654.02 | +15.03          | ALFOSC/NOT    | $4 \times 900$  |
| 2019 Jun 30          | 58664.28 | +25.18          | GMOS-N/Gemini | $2 \times 1200$ |

**Note.** The phase is relative to the epoch of *g*-band maximum in the SN rest frame.

Follow-up spectra (Table 2) were obtained with the Alhambra Faint Object Spectrograph and Camera (ALFOSC) on NOT during five epochs between  $-0.8$  and  $+15.0$  days relative to *g*-band maximum, using grism 4 (3300–9600 Å) and a  $1''/3$  slit yielding a resolution  $R \approx 400$ . The extractions, wavelength, and flux calibrations were applied using custom IRAF scripts. A Gemini spectrum was obtained on  $+25.2$  days using the GMOS-N instrument. The GMOS spectrum, obtained using the R400 grating ( $R \approx 1900$ ) and a  $1''$  slit, was reduced with the Gemini IRAF package. Synthetic photometry was computed for the spectra using the Synthetic Magnitudes from Spectra code (SMS; Inserra et al. 2018), and the spectral fluxes were scaled to match the multiband Pan-STARRS1 photometry. Pan-STARRS1 images of SN 2019gsc are shown in Figure 1, along with the NOT  $r$ -band image and slit positions for the NOT spectra.

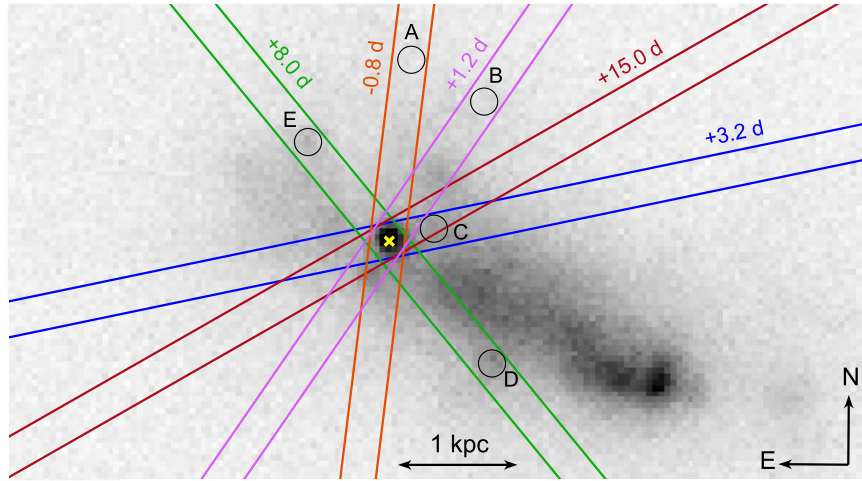
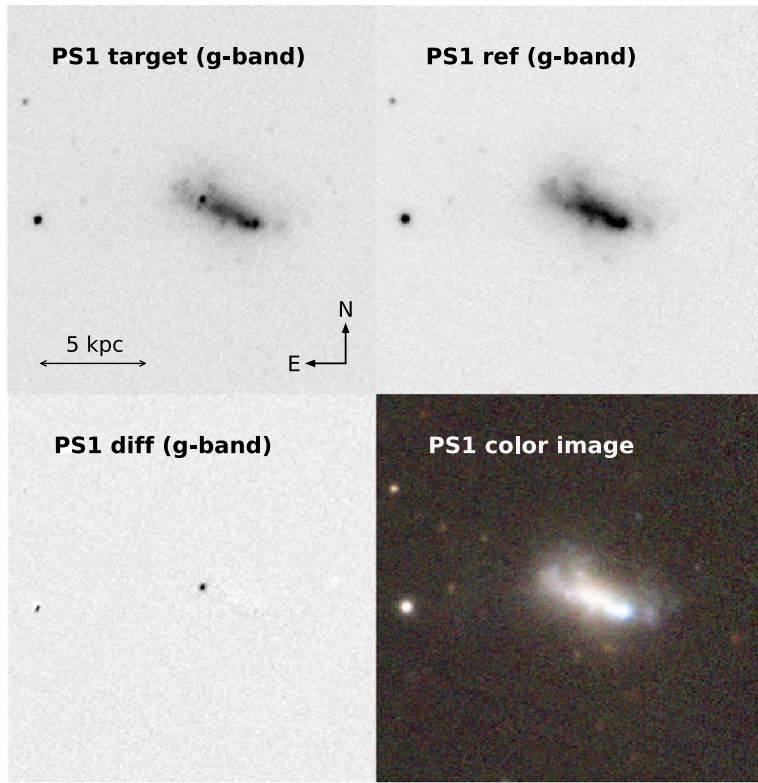


**Figure 1.** Top: Pan-STARRS target, reference, difference, and color composite images of the field for SN 2019gsc. The *g*-band target image was acquired on MJD 58643.3 (+4.4 days since *g*-band maximum). Bottom: NOT *r*-band image of SN 2019gsc (cross) and its host galaxy, taken on MJD 58638.0 (−0.8 days since *g*-band maximum). Also shown is the orientation of the slits of the NOT spectra. The phase is relative to the epoch of *g*-band maximum in the SN rest frame. The circles mark those regions with bright nebular emission lines used to estimate the gal metallicity (Section 4.1).

### 3. Light Curves and Luminosity

#### 3.1. Line-of-sight Reddening

In general, colors of SNe Ia around maximum light and the color evolution after maximum can be used to estimate the host galaxy extinction (e.g., Wang et al. 2005; Folatelli et al. 2010; Burns et al. 2014). However, these empirical relations are unreliable for SNe Ia due to a large scatter in their intrinsic colors (Foley et al. 2013).

From the NASA/IPAC Extragalactic Database, the Galactic extinction along the line of sight for the host galaxy SBS 1436 +529A is  $A_V = 0.026$  mag (Schlafly & Finkbeiner 2011), for a standard reddening law with  $R_V = 3.1$ . We do not detect any

obvious Na I absorption in the optical spectra at the host galaxy redshift, suggesting a low host reddening for SN 2019gsc. Thus, we assume a total extinction of  $E(B - V)_{\text{tot}} = E(B - V)_{\text{MW}} = 0.01$  mag for SN 2019gsc. For SN 2008ha, we consider  $E(B - V)_{\text{tot}} = E(B - B)_{\text{MW}} = 0.08$  mag, following Foley et al. (2009). In the case of SN 2010ae, prominent Na I absorption in the spectra at the host galaxy redshift indicated a significant, albeit highly uncertain host galaxy extinction of  $E(B - V)_{\text{host}} = 0.50 \pm 0.42$  mag, with  $E(B - V)_{\text{tot}} = 0.62 \pm 0.42$  mag (Stritzinger et al. 2014). Correcting the magnitudes for the extinction values stated above, we note that the (*g* − *r*) color evolution of SNe 2019gsc

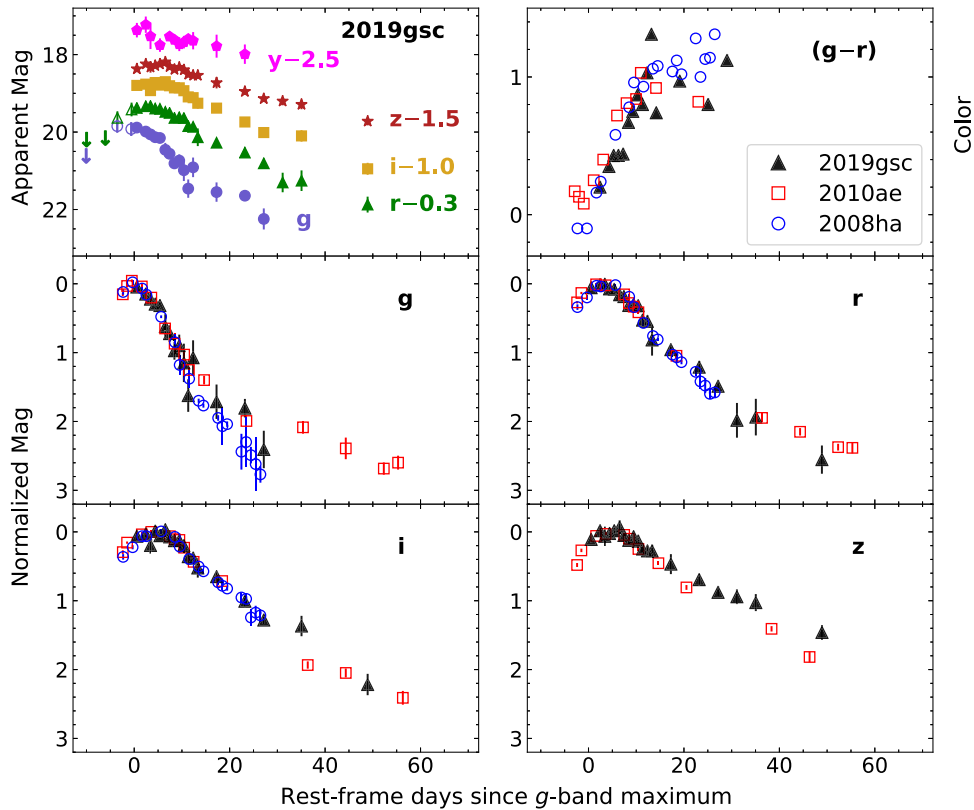


**Figure 2.** Pan-STARRS *grizy* light curves of SN 2019gsc (top left panel), plotted along with ZTF *g* and ZTF *r* filter magnitudes (open symbols) and ZTF upper limits (downward-pointing arrows). Also plotted is the  $(g - r)$  color evolution of SNe 2019gsc, 2010ae and 2008ha (top right panel), corrected for extinction as described in Section 3.1. Panels 3–6 show the light curve comparison in the *griz* bands between SN 2019gsc and the faint Iax events 2008ha and 2010ae (Stritzinger et al. 2014).

and 2008ha is very similar. Adopting a moderate extinction value of  $E(B - V)_{\text{tot}} \approx 0.30$  mag, we see that the  $(g - r)$  color evolution of SN 2010ae matches that of the other two events more closely (Figure 2). Thus, we adopt  $E(B - V)_{\text{tot}} = 0.30$  mag for SN 2010ae in the subsequent analysis.

### 3.2. Pan-STARRS1 Light Curves

The Pan-STARRS1 (PS1) *grizy*<sub>P1</sub> light curves of SN 2019gsc are shown in Figure 2 (top left panel). The peak magnitudes and epochs in different bands and the post-maximum decline rates were estimated by fitting lower-order polynomials to the light curves. SN 2019gsc peaked in the *g* band on MJD  $58638.8 \pm 0.4$ , at an apparent AB magnitude of  $m_g = 19.88 \pm 0.10$ . The peak in the redder *riz* bands occurred at later epochs, at +2.3, +3.9, and +4.4 days since *g*-band maximum, respectively. The light curves of SNe Iax are known to be quite heterogeneous (Magee et al. 2016). SNe Iax typically show a fast decline in their light curves relative to normal SNe Ia, with decline rates comparable to the transitional and subluminous SN 1991bg-like population (Stritzinger et al. 2015).

The *griz* light curves of SN 2019gsc are compared with those of SNe 2010ae and 2008ha (Stritzinger et al. 2014), two of the faintest known Iax events, in Figure 2 (panels 3–6). The light curves were normalized and shifted along the time axis to correspond to the epoch of their respective *g*-band maxima.

### 3.3. Bolometric Light Curve and Explosion Parameters

The peak absolute magnitudes of SN 2019gsc corrected for extinction (Section 3.1) and assuming a distance modulus of 33.60 mag (Section 2),  $M_g^{\text{peak}} = -13.75 \pm 0.23$ , and  $M_r^{\text{peak}} = -13.97 \pm 0.16$ , making it one of the faintest SNe Iax ever observed, if not the faintest.

The bolometric light curve of SN 2019gsc was calculated from the multiband PS1 photometry using the `SuperBol` code (Nicholl 2018). To account for missing flux in the UV and IR bands, the code also performs a blackbody fit to the spectral energy distribution (SED) for each epoch, where a suppression factor for the UV flux can be supplied to account for line-blanketing effects. The quasi-bolometric light curve of SN 2019gsc (3900–11000 Å), along with the full blackbody bolometric fit (1000–25000 Å), is shown in Figure 3. We recalculated the blackbody bolometric light curves of SNe 2008ha and 2010ae from the data in Foley et al. (2009) and Stritzinger et al. (2014) for consistency. Distance moduli of  $\mu = 31.64$  mag for SN 2008ha (Foley et al. 2009) and  $\mu = 30.58$  mag for SN 2010ae (Stritzinger et al. 2014) were assumed, along with extinction corrections to the broadband as discussed in Section 3.1. SN 2019gsc is an exceptionally low luminosity event, with a peak bolometric luminosity of  $L_{\text{peak}} \approx 5.1_{-0.7}^{+0.8} \times 10^{40}$  erg s<sup>-1</sup> for the quasi-bolometric light curve, and  $L_{\text{peak}} \approx 7.4_{-1.0}^{+1.1} \times 10^{40}$  erg s<sup>-1</sup> for the full blackbody bolometric light curve (Figure 3).

The bolometric light curves were fit with an Arnett model (Arnett 1982), as formulated by Valenti et al. (2008), to estimate the explosion parameters such as <sup>56</sup>Ni mass ( $M_{\text{Ni}}$ ), ejecta mass ( $M_{\text{ej}}$ ), and kinetic energy ( $E_{51}$ , expressed in units of

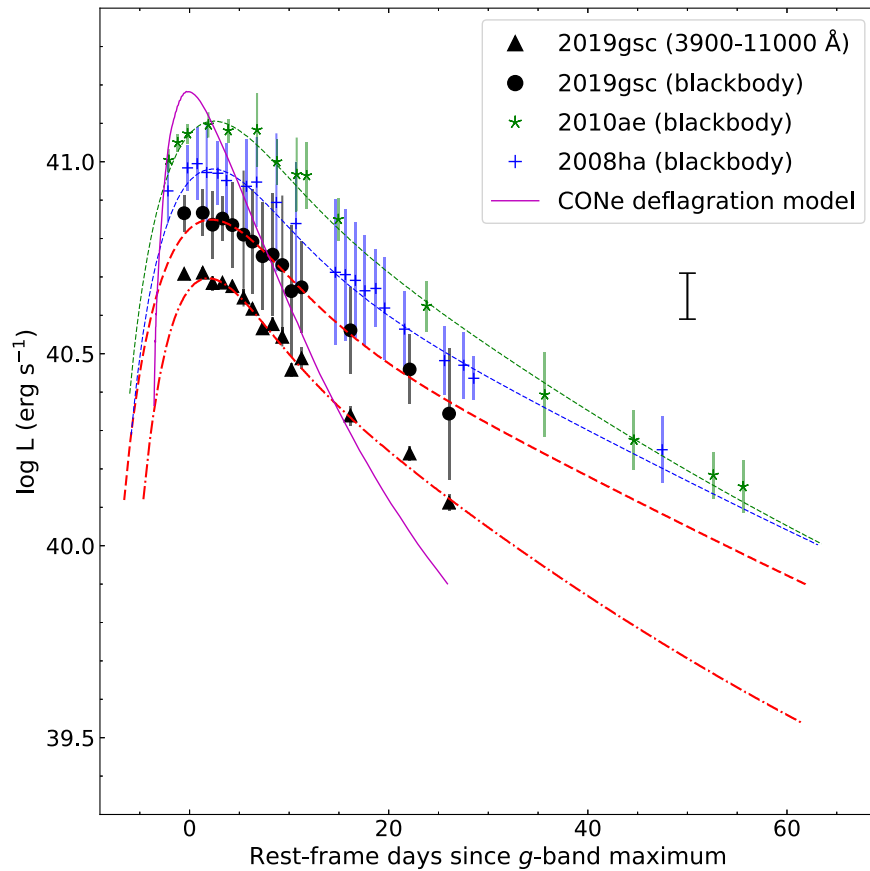


**Figure 3.** Quasi-bolometric (3900–11000 Å) and blackbody bolometric (1000–25000 Å) light curves of SN 2019gsc, along with the blackbody bolometric light curves of SNe 2010ae and 2008ha for comparison. The bolometric light curves were calculated using a blackbody fit to the SEDs at individual epochs, as described in the text. The dashed lines indicate the best-fitting Arnett-Valenti models. The solid line indicates the angle-averaged synthetic bolometric light curve for the hybrid CONe WD deflagration model (Kromer et al. 2015). The error bar below the legend represents the systematic uncertainty on the luminosity for  $\pm 0.15$  mag uncertainty on the distance modulus.

$10^{51}$  erg). The model assumes homologous expansion, spherical symmetry, optically thick ejecta, and no mixing for  $^{56}\text{Ni}$ . The free parameters were  $M_{\text{Ni}}$ ,  $M_{\text{ej}}$ , and the rise time  $t_{\text{rise}}$  of the bolometric light curve, while we fixed the optical opacity  $\kappa_{\text{opt}} = 0.1 \text{ cm}^2 \text{ g}^{-1}$ . The photospheric velocity was fixed at  $v_{\text{ph}} = 3500 \text{ km s}^{-1}$  (see Section 4). Fitting the quasi-bolometric (3900–11000 Å) as well as the blackbody bolometric (1000–25000 Å) light curve yields  $M_{\text{Ni}} \sim (1.4\text{--}2.4) \times 10^{-3} M_{\odot}$ ,  $M_{\text{ej}} \sim 0.13\text{--}0.22 M_{\odot}$ , and  $E_{51} \sim 0.01\text{--}0.02$ . The fit favors a low rise time of  $t_{\text{rise}} \approx 10$  days, similar to that inferred for SNe 2008ha (Foley et al. 2009) and 2010ae (Magee et al. 2016).

We note that the peak quasi-bolometric flux is  $\sim 70\%$  of the peak blackbody bolometric flux for SN 2019gsc, indicating a significant contribution from the UV and NIR. In contrast, the UV and NIR fraction was seen to be only  $\sim 10\%$  for the transitional Ia SN 2011iv (Gall et al. 2018). This could imply either a higher intrinsic UV contribution for 2019gsc, or that the UV suppression factor fed to SuperBol was too low, or both.

A similar analysis on the bolometric light curves of SNe 2008ha and 2010ae yields  $M_{\text{Ni}} \sim 3 \times 10^{-3} M_{\odot}$ ,  $M_{\text{ej}} \sim 0.1\text{--}0.2 M_{\odot}$ , and  $E_{51} \sim 0.01$ ;  $M_{\text{Ni}} = (3\text{--}4) \times 10^{-3} M_{\odot}$ ,  $M_{\text{ej}} \sim 0.2\text{--}0.3 M_{\odot}$ , and  $E_{51} \sim 0.03\text{--}0.05$ , respectively.

#### 4. Spectral Modeling

The spectra of SN 2019gsc (Figure 4) resemble the faint SNe Iax 2008ha (Foley et al. 2009; Valenti et al. 2009) and 2010ae (Stritzinger et al. 2014). The spectra of SNe 2008ha and 2010ae were downloaded from the Weizmann interactive supernova data repository (WISeREP,<sup>11</sup> Yaron & Gal-Yam 2012). The earliest spectrum ( $-0.8$  day) exhibits a blue continuum with  $T_{\text{bb}} \approx 11000 \text{ K}$  and Si II  $\lambda 6355$  velocity of  $\sim 3800 \text{ km s}^{-1}$ , decreasing to  $T_{\text{bb}} \approx 8000 \text{ K}$  and velocity of  $\sim 1600 \text{ km s}^{-1}$  at  $+15$  days.

We used the 1D radiative transfer code TARDIS (Kerzendorf & Sim 2014; Kerzendorf et al. 2018) to produce synthetic spectra to compare with the observed data. TARDIS has been previously used to model spectral sequences of SNe Iax in order to investigate the chemical structure (Magee et al. 2016, 2017; Barna et al. 2017, 2018) and presence of helium in the ejecta (Magee et al. 2019). TARDIS takes a model for the ejecta with arbitrary density and abundance profiles as input, along with a luminosity and time since explosion. A sharp photosphere emitting a blackbody continuum is assumed, and the region above the photosphere is divided into multiple, spherically symmetric cells. The photospheric approximation assumed in TARDIS limits its applicability to the early phase. The synthetic spectrum is calculated by iterative computation

<sup>11</sup> <https://wiserep.weizmann.ac.il>

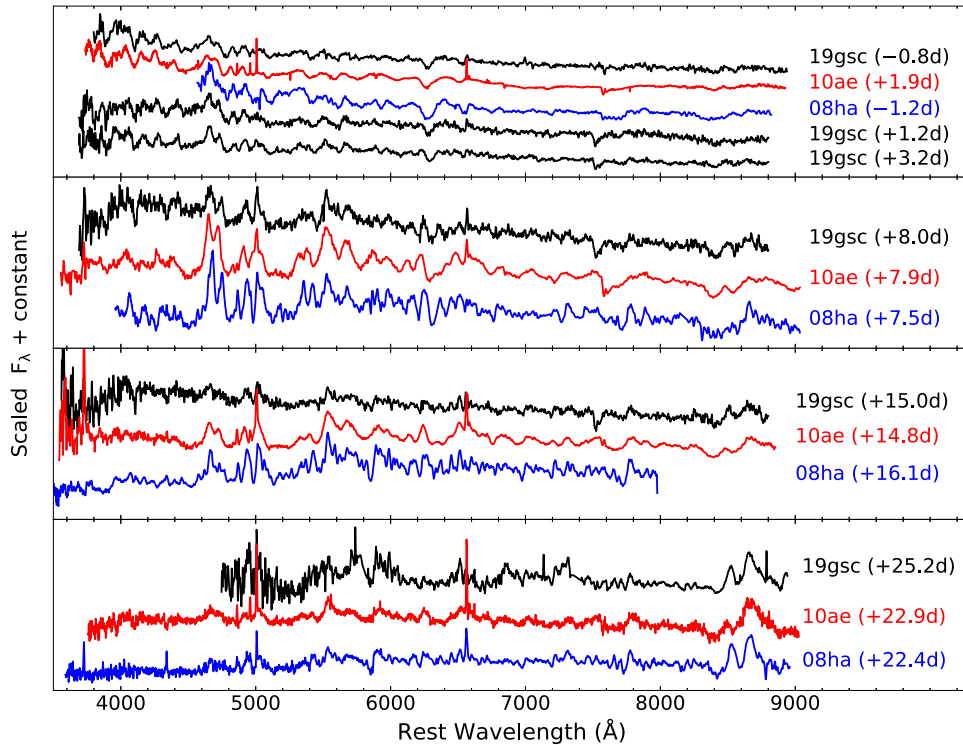


**Figure 4.** Spectral evolution of SN 2019gsc from  $-0.8$  to  $+25.2$  days, compared to SNe 2010ae (Stritzinger et al. 2014) and 2008ha (Foley et al. 2009; Valenti et al. 2009) at similar epochs. The spectra were corrected for redshift and line-of-sight extinction as described in the text.

of the ionization and excitation states in each of the cells (Kerzendorf & Sim 2014).

For each spectral epoch of SN 2019gsc in our fit, only the time-dependent parameters (luminosity, time since explosion, inner boundary of the computation volume, and mass fractions of radioactive isotopes) were varied. The luminosity supplied to the input file was calculated by interpolating the quasi-bolometric light curve at the desired epochs. An exponential density profile was adopted for the SN ejecta, where the density profile is a function of velocity and time since explosion, expressed as

$$\rho(v, t_{\text{exp}}) = \rho_0 (t_0/t_{\text{exp}})^3 e^{-v/v_0}.$$

Here, we set  $t_0 = 2$  days,  $\rho_0 = 2 \times 10^{-11}$  g cm $^{-3}$ , and  $v_0 = 3000$  km s $^{-1}$ . The epoch of explosion,  $t_{\text{exp}}$ , was assumed to be MJD  $\sim 58630.5$ , roughly the mean of the two deep ZTF nondetections prior to discovery. For the abundance, we adopt the simplest case of a uniform abundance profile in each spherical cell. The outer velocity boundary of the models was set to  $6000$  km s $^{-1}$ . The model is composed primarily of carbon and oxygen, together constituting  $\sim 96\%$  of the total mass.

The four early spectra of SN 2019gsc modeled with TARDIS (7.5–16.4 days past explosion) are shown in Figure 5, along with the model synthetic spectra. The continuum is well reproduced in the synthetic spectra, along with the primary spectral features of IMEs such as O I, Si II, and S II. However, Fe features around  $5000$  Å are not fit well, especially in the spectrum observed 9.5 days after explosion. Ca II features are also identified in the spectra (Figure 5). In addition, introducing small amounts of Cr, Ti, and Sc qualitatively improves the fit in the  $4000$ – $5000$  Å region.

The best-fit parameters and mass fractions of various elements in the models are listed in Table 3. In addition to

the tabulated chemical elements, small amounts ( $X \leq 10^{-5}$ ) of Na, Ca, Cr, Sc, and Ti were also used.

The total mass in our TARDIS model, summed over all the spherical shells in the computation volume amounts to  $\approx 0.01 M_{\odot}$ , a factor of 10 lower than the ejecta mass estimate from the bolometric light curve. This is consistent, since a significant amount of mass is expected to be below the effective photosphere delineating the optically thick and thin regions of the ejecta. The upper limit on the mass fraction of  $^{56}\text{Ni}$  from the model is  $\lesssim 1\%$ , or  $M_{\text{Ni}} \lesssim 10^{-4} M_{\odot}$ , consistent with the  $^{56}\text{Ni}$  mass estimate from the bolometric light curve.

#### 4.1. Host Metallicity

While SNe Iax mostly do not appear to correlate with low-metallicity environments (Magee et al. 2017), both of the very low luminosity events (SN 2008ha and SN 2010ae) were associated with low-metallicity host galaxies. Foley et al. (2009) estimated an oxygen abundance of  $12 + \log(\text{O}/\text{H}) = 8.16 \pm 0.15$  dex for SN 2008ha and from the N2 and O3N2 indicators of Pettini & Pagel (2004), while Stritzinger et al. (2014) estimated  $12 + \log(\text{O}/\text{H}) = 8.40 \pm 0.12$  dex (N2) and  $8.34 \pm 0.14$  dex (O3N2).

In order to estimate the host metallicity for SN 2019gsc, we used the NOT spectra obtained at different dates. All spectra had different slit orientations, as they were obtained at parallactic angle but at different hour angles (Figure 1). Regions A–E were dominated by strong nebular emission lines. The [N II] lines are not significantly detected in regions A, B, and C, leading to upper limits of  $12 + \log(\text{O}/\text{H}) < 8.10$  (8.07) dex,  $12 + \log(\text{O}/\text{H}) < 8.18$  (8.13) dex; and  $12 + \log(\text{O}/\text{H}) < 8.35$  (8.18) dex, calibrated on the N2 (O3N2) scales, respectively. In regions D and E, [N II] is marginally detected, allowing us to estimate a metallicity of  $12 + \log(\text{O}/\text{H})$

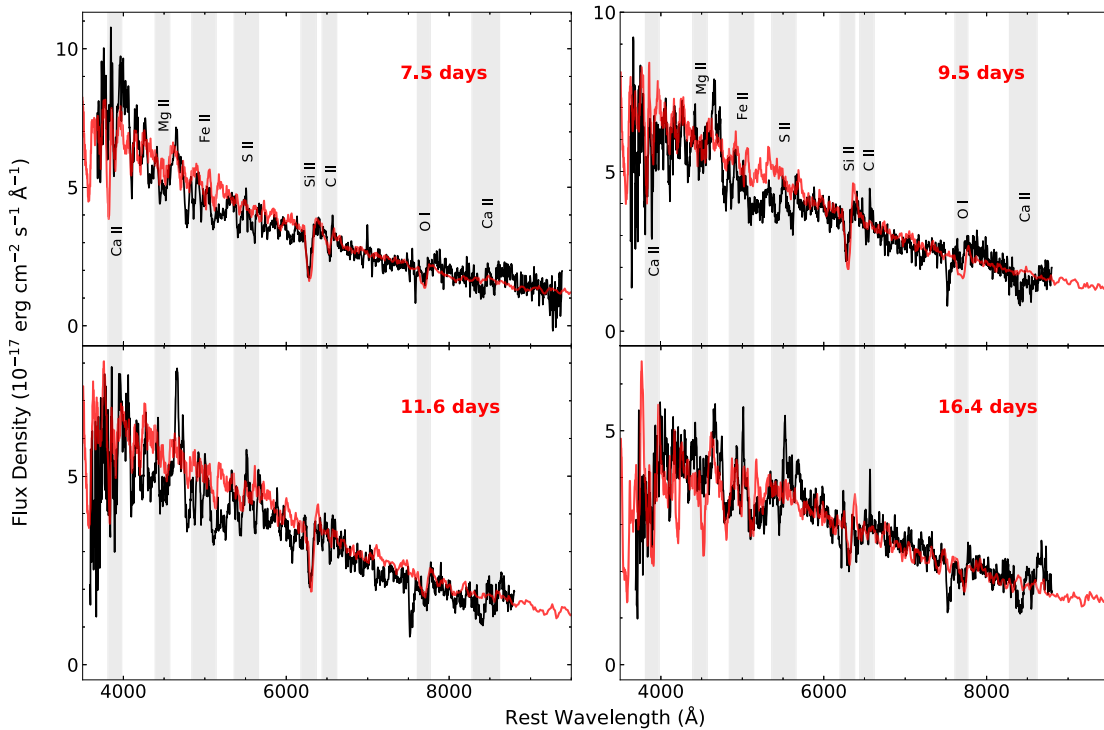


**Figure 5.** NOT spectra (in black) of SN 2019gsc in the photospheric phase (7.5–16.4 days past explosion), plotted along with the synthetic spectra (in red) generated using TARDIS at the corresponding epoch. Shaded regions indicate prominent features in the spectra. The epochs correspond to the spectra in Figure 4 at  $-0.8$ ,  $+1.2$ ,  $+3.2$ , and  $+8.0$  days since  $g$ -band maximum.

$H) = 8.10 \pm 0.06$  dex (N2),  $12 + \log(O/H) = 8.08 \pm 0.06$  dex (O3N2) for region E; and  $12 + \log(O/H) = 7.81 \pm 0.19$  dex (N2),  $12 + \log(O/H) = 7.86 \pm 0.08$  dex (O3N2) for region D. These values suggest a very metal-poor environment (15% solar) for SN 2019gsc, among the most metal-poor environments for the Iax sample (Lyman et al. 2018).

In addition, the extracted spectra at regions A, B, D, and E also show very strong  $H\alpha$  and  $[O\ III] \lambda 5007$  emission lines (equivalent widths of  $\sim 100$ – $200$  Å), suggesting that SN 2019gsc is in proximity to regions undergoing a starburst.

## 5. Discussion and Conclusions

SN 2019gsc is probably the least luminous supernova-like transient discovered, with a peak luminosity  $M_g \approx -13.8 \pm 0.2$  mag. It shows strong photometric and spectroscopic similarities to SNe 2008ha and 2010ae, which had peak luminosities of  $M_g = -14.01 \pm 0.14$ ,  $-13.54 \gtrsim M_g \gtrsim -15.33$  (Stritzinger et al. 2014). The explosion parameters estimated from the bolometric light curves of all three are also similar. Fitting the bolometric light curve of SN 2019gsc with an energy deposition model suggests  $M_{Ni} \sim 2 \times 10^{-3} M_\odot$ ,  $M_{ej} \sim 0.2 M_\odot$ , and kinetic energy  $E_{51} \sim 0.01$ – $0.02$ . Our estimates for the luminosity, decline rates, and explosion parameters for SN 2019gsc are consistent, within uncertainties, with those presented in Tomasella et al. (2002). Furthermore, somewhat remarkably, all three occur in blue, star-forming host galaxies, with indications of moderately low to extremely low metallicity host environments. These three SNe represent the extreme low-luminosity and low-energy end of the population of supernovae classed as type Iax. However the peculiar properties that they all have in common

now raise the question if they are physically distinct explosions from the bulk of the SN Iax population.

Pure deflagrations of WDs (Branch et al. 2004; Phillips et al. 2007) have been proposed to account for the low explosion energy and luminosity of SNe Iax in general. Hydrodynamic 3D simulations of weak deflagrations can fail to completely unbind the WD and are predicted to leave a “bound” remnant behind (Jordan et al. 2012; Kromer et al. 2013). However, the extremely low luminosities of SNe 2019gsc, 2010ae, and 2008ha place them below the range of ejected  $^{56}\text{Ni}$  masses predicted by existing sets of deflagration models for CO WDs (Jordan et al. 2012; Fink et al. 2014). One potential means of obtaining an extremely low  $^{56}\text{Ni}$  ejected mass was proposed by Kromer et al. (2015). A deflagration simulation involving a near- $M_{Ch}$  hybrid carbon–oxygen–neon (CONE) WD yielded  $M_{Ni} \sim 3 \times 10^{-3} M_\odot$ , consistent with the luminosity of SNe 2019gsc, 2010ae, and 2008ha. A very low total ejecta mass resulted from these simulations ( $M_{ej} \sim 0.01 M_\odot$ ), which is a factor 20 lower than the mass we infer from the light curves. The comparison in Figure 3 illustrates the point that the ratio of  $M_{Ni}/M_{ej}$  from the Kromer et al. (2015) CONE WD explosion simulation is significantly higher than that inferred from the observed light curves. The CO deflagrations of Fink et al. (2014) produce higher ejecta masses, more compatible with the data (e.g., their N3def model), but the  $^{56}\text{Ni}$  mass from that simulation is too high. A uniform composition is sufficient for satisfactory TARDIS fits to the early spectra. This favors a mixed ejecta rather than a layered ejecta composition, since the turbulent mixing in deflagration is expected to prevent distinct velocity layers containing different elements (Gamezo et al. 2003). However, more complex, layered ejecta structures are not ruled out.

**Table 3**  
Best-fit Parameters and Mass Fractions of Different Chemical Elements in the TARDIS Models for SN 2019gsc

| $t_{\text{exp}}$<br>(days) | $L$<br>( $\log L_{\odot}$ ) | $v_{\text{inner}}$<br>( $\text{km s}^{-1}$ ) | $X(\text{C})$ | $X(\text{O})$ | $X(\text{Mg})$ | $X(\text{Si})$ | $X(\text{S})$ | $X(\text{Fe})$     | $X(\text{Co})$       | $X(\text{Ni})$       |
|----------------------------|-----------------------------|--|---------------|---------------|----------------|----------------|---------------|--------------------|----------------------|----------------------|
| 7.5                        | 7.32                        | 2600   | 0.75          | 0.21          | 0.01           | 0.02           | 0.005         | $2 \times 10^{-4}$ | $2.8 \times 10^{-4}$ | $2.1 \times 10^{-4}$ |
| 9.5                        | 7.35                        | 2300   | 0.75          | 0.21          | 0.01           | 0.02           | 0.005         | $2 \times 10^{-4}$ | $3.1 \times 10^{-4}$ | $1.7 \times 10^{-4}$ |
| 11.6                       | 7.34                        | 2000   | 0.75          | 0.21          | 0.01           | 0.02           | 0.005         | $2 \times 10^{-4}$ | $3.4 \times 10^{-4}$ | $1.4 \times 10^{-4}$ |
| 16.4                       | 7.23                        | 1600   | 0.75          | 0.21          | 0.01           | 0.02           | 0.005         | $2 \times 10^{-4}$ | $3.9 \times 10^{-4}$ | $8 \times 10^{-5}$   |

**Note.**  $v_{\text{inner}}$  denotes the inner boundary of the computation volume and  $t_{\text{exp}}$  is the time since explosion. The emergent luminosity ( $L$ ) was fixed by interpolating the bolometric light curve at the relevant epochs.

Binary population synthesis studies have shown that hybrid CONe WDs with helium-burning donors have short delay times of 30–180 Myr (Wang et al. 2014; Kromer et al. 2015). This is consistent with the fact that Iax events are generally associated with young stellar populations (Foley et al. 2014; McCully et al. 2014b; Lyman et al. 2018). In addition, low-metallicity stars are expected to form higher-mass WDs (Kistler et al. 2013), implying a shorter time required to bring them to explosion. The fact that all three of these extremely low luminosity Iax are in apparently young stellar populations suggests this channel might be promising.

Our observations do not yet rule out a massive star origin for these faint events. A weak core collapse of a stripped, massive star involving fallback on to the central remnant was proposed for SN 2008ha (Valenti et al. 2009; Moriya et al. 2010).

The discovery of a blue point source in pre-explosion *HST* images of the type Iax SN 2012Z led McCully et al. (2014b) to argue for a helium-rich donor as the binary companion to the WD, rather than a massive star. This scenario is consistent with the detection of helium features in the spectra of potential Iax events 2004cs and 2007J (Foley et al. 2013, 2016), although their association with SNe Iax has been disputed (White et al. 2015). Although we do not invoke helium in our TARDIS model, this does not rule out its presence in the ejecta (see Magee et al. 2019).

Future detection and characterization of “bound” remnants at the sites of Iax explosions (Zhang et al. 2019), and unambiguous spectroscopic confirmation of the companions of Iax progenitors as helium stars, would help resolve these questions. Further theoretical simulations of deflagrations are required to explore if the model parameters can produce the observed  $M_{\text{Ni}}/M_{\text{ej}}$  ratio and better reproduce the observed light curves. The balance between how much  $^{56}\text{Ni}$  is trapped in a bound object compared to how much is ejected needs further investigation. In addition, the energy radiated from a “bound” object may be slower than from a freely expanding remnant, which would help slow the light curve evolution.

Data are from the Asteroid Terrestrial-impact Last Alert System project (NASA grants NN12AR55G, 80NSSC18K0284, and 80NSSC18K1575), byproducts of the NEO search include images and catalogs from the survey area, through the contributions of the University of Hawaii Institute for Astronomy, the Queen’s University Belfast, the Space Telescope Science Institute, and the South African Astronomical Observatory. Pan-STARRS is supported by the NASA Grants, including No. NNX14AM74G through the SSO NEO Observations Program. S.J.S., S.S., S.A.S., D.R.Y., and K.W.S. acknowledge STFC Grants ST/P000312/1, ST/N006550/1, ST/N002520/1, and ST/S006109/1. S.S. thanks B. Barna and

M. R. Magee for useful discussions. G.L. and D.B.M. acknowledge research grant 19054 from VILLUM FONDEN. C.G. acknowledges VILLUM FONDEN research grant 25501. This work was supported by a VILLUM FONDEN Investigator grant 16599 to J.H. K.A.A. acknowledges DNR132. We thank Jonatan Selsing for help with NOT spectroscopic reductions. Nordic Optical Telescope (programs 59-008 and 59-509), operated by the NOT Scientific Association at the Observatory del Roque de los Muchachos, La Palma, Spain, of the IAC. Gemini observatory (program GN-2019A-Q-126) is operated by the Association of Universities for Research in Astronomy, Inc., under a cooperative agreement with the NSF on behalf of the Gemini partnership: the National Science Foundation (United States), National Research Council (Canada), CONICYT (Chile), Ministerio de Ciencia, Tecnología e Innovación Productiva (Argentina), Ministério da Ciência, Tecnologia e Inovação (Brazil), and Korea Astronomy and Space Science Institute (Republic of Korea). We made use of TARDIS supported by the Google Summer of Code and ESA’s Summer of Code in Space.

*Facilities:* ATLAS, Pan-STARRS, NOT, Gemini-North.

*Software:* <https://github.com/mnicholl/superbol>.

### ORCID iDs

Shubham Srivastav  <https://orcid.org/0000-0003-4524-6883>  
 Stephen J. Smartt  <https://orcid.org/0000-0002-8229-1731>  
 Giorgos Leloudas  <https://orcid.org/0000-0002-8597-0756>  
 Mark E. Huber  <https://orcid.org/0000-0003-1059-9603>  
 Ken Chambers  <https://orcid.org/0000-0001-6965-7789>  
 Daniele B. Malesani  <https://orcid.org/0000-0002-7517-326X>  
 Jens Hjorth  <https://orcid.org/0000-0002-4571-2306>  
 Stuart A. Sim  <https://orcid.org/0000-0002-9774-1192>  
 Katie Auchettl  <https://orcid.org/0000-0002-4449-9152>  
 Johan P. U. Fynbo  <https://orcid.org/0000-0002-8149-8298>  
 Christa Gall  <https://orcid.org/0000-0002-8526-3963>  
 Owen R. McBrien  <https://orcid.org/0000-0001-8049-4036>  
 Ken W. Smith  <https://orcid.org/0000-0001-9535-3199>  
 David R. Young  <https://orcid.org/0000-0002-1229-2499>

### References

- Argudo-Fernández, M., Verley, S., Bergond, G., et al. 2015, *A&A*, 578, A110  
 Arnett, W. D. 1982, *ApJ*, 253, 785  
 Barna, B., Szalai, T., Kerzendorf, W. E., et al. 2018, *MNRAS*, 480, 3609  
 Barna, B., Szalai, T., Kromer, M., et al. 2017, *MNRAS*, 471, 4865  
 Bellm, E. C., Kulkarni, S. R., Graham, M. J., et al. 2019, *PASP*, 131, 018002  
 Branch, D., Baron, E., Thomas, R. C., et al. 2004, *PASP*, 116, 903  
 Burns, C. R., Stritzinger, M., Phillips, M. M., et al. 2014, *ApJ*, 789, 32  
 Chambers, K. C., Magnier, E. A., Metcalfe, N., et al. 2016, arXiv:1612.05560  
 Fink, M., Kromer, M., Seitenzahl, I. R., et al. 2014, *MNRAS*, 438, 1762  
 Folatelli, G., Phillips, M. M., Burns, C. R., et al. 2010, *AJ*, 139, 120

- Foley, R. J., Brown, P. J., Rest, A., et al. 2010, *ApJL*, **708**, L61
- Foley, R. J., Challis, P. J., Chornock, R., et al. 2013, *ApJ*, **767**, 57
- Foley, R. J., Chornock, R., Filippenko, A. V., et al. 2009, *AJ*, **138**, 376
- Foley, R. J., Jha, S. W., Pan, Y.-C., et al. 2016, *MNRAS*, **461**, 433
- Foley, R. J., McCully, C., Jha, S. W., et al. 2014, *ApJ*, **792**, 29
- Gall, C., Stritzinger, M. D., Ashall, C., et al. 2018, *A&A*, **611**, A58
- Gamezo, V. N., Khokhlov, A. M., Oran, E. S., Chtchelkanova, A. Y., & Rosenberg, R. O. 2003, *Sci*, **299**, 77
- Hamuy, M., Phillips, M. M., Suntzeff, N. B., et al. 1996, *AJ*, **112**, 2391
- Howell, D. A. 2011, *NatCo*, **2**, 350
- Hoyle, F., & Fowler, W. A. 1960, *ApJ*, **132**, 565
- Insera, C., Smartt, S. J., Gall, E. E. E., et al. 2018, *MNRAS*, **475**, 1046
- Jha, S. W. 2017, in *Handbook of Supernovae*, ed. A. Alsabti & P. Murdin (Berlin: Springer), 375
- Jordan, G. C. I., Perets, H. B., Fisher, R. T., & van Rossum, D. R. 2012, *ApJL*, **761**, L23
- Kerzendorf, W., Nöbauer, U., Sim, S., et al. 2018, tardis-sn/tardis: TARDIS v2.0.2 Release, v2.0.2, Zenodo, doi:10.5281/zenodo.1292315
- Kerzendorf, W. E., & Sim, S. A. 2014, *MNRAS*, **440**, 387
- Kistler, M. D., Stanek, K. Z., Kochanek, C. S., Prieto, J. L., & Thompson, T. A. 2013, *ApJ*, **770**, 88
- Kromer, M., Fink, M., Stanishev, V., et al. 2013, *MNRAS*, **429**, 2287
- Kromer, M., Ohlmann, S. T., Pakmor, R., et al. 2015, *MNRAS*, **450**, 3045
- Leloudas, G., Malesani, D. B., Fynbo, J. P. U., et al. 2019, *TNSAN*, **25**, 1
- Li, W., Filippenko, A. V., Chornock, R., et al. 2003, *PASP*, **115**, 453
- Lyman, J. D., Taddia, F., Stritzinger, M. D., et al. 2018, *MNRAS*, **473**, 1359
- Magee, M. R., Kotak, R., Sim, S. A., et al. 2016, *A&A*, **589**, A89
- Magee, M. R., Kotak, R., Sim, S. A., et al. 2017, *A&A*, **601**, A62
- Magee, M. R., Sim, S. A., Kotak, R., Maguire, K., & Boyle, A. 2019, *A&A*, **622**, A102
- Magnier, E. A., Chambers, K. C., Flewelling, H. A., et al. 2016a, arXiv:1612.05240
- Magnier, E. A., Sweeney, W. E., Chambers, K. C., et al. 2016b, arXiv:1612.05244
- Maoz, D., Mannucci, F., & Nelemans, G. 2014, *ARA&A*, **52**, 107
- McClelland, C. M., Garnavich, P. M., Galbany, L., et al. 2010, *ApJ*, **720**, 704
- McCully, C., Jha, S. W., Foley, R. J., et al. 2014a, *ApJ*, **786**, 134
- McCully, C., Jha, S. W., Foley, R. J., et al. 2014b, *Natur*, **512**, 54
- Moriya, T., Tominaga, N., Tanaka, M., et al. 2010, *ApJ*, **719**, 1445
- Narayan, G., Foley, R. J., Berger, E., et al. 2011, *ApJL*, **731**, L11
- Nicholl, M. 2018, *RNAAS*, **2**, 230
- Nomoto, K., Thielemann, F.-K., & Yokoi, K. 1984, *ApJ*, **286**, 644
- Pettini, M., & Pagel, B. E. J. 2004, *MNRAS*, **348**, L59
- Phillips, M. M. 1993, *ApJL*, **413**, L105
- Phillips, M. M., Li, W., Frieman, J. A., et al. 2007, *PASP*, **119**, 360
- Schlafly, E. F., & Finkbeiner, D. P. 2011, *ApJ*, **737**, 103
- Smartt, S. J., McBrien, O., Smith, K. W., et al. 2019, *TNSAN*, **23**, 1
- Smith, K. W., Williams, R. D., Young, D. R., et al. 2019, *RNAAS*, **3**, 26
- Stritzinger, M. D., Hsiao, E., Valenti, S., et al. 2014, *A&A*, **561**, A146
- Stritzinger, M. D., Valenti, S., Hoeflich, P., et al. 2015, *A&A*, **573**, A2
- Tomasella, L., Cappellaro, E., Benetti, S., et al. 2016, *MNRAS*, **459**, 1018
- Tomasella, L., Stritzinger, M., Benetti, S., et al. 2020, arXiv:2002.00393
- Tonry, J. L., Denneau, L., Heinze, A. N., et al. 2018, *PASP*, **130**, 064505
- Tonry, J. L., Stubbs, C. W., Lykke, K. R., et al. 2012, *ApJ*, **750**, 99
- Valenti, S., Benetti, S., Cappellaro, E., et al. 2008, *MNRAS*, **383**, 1485
- Valenti, S., Pastorello, A., Cappellaro, E., et al. 2009, *Natur*, **459**, 674
- Wang, B., Meng, X., Liu, D. D., Liu, Z. W., & Han, Z. 2014, *ApJL*, **794**, L28
- Wang, X., Wang, L., Zhou, X., Lou, Y.-Q., & Li, Z. 2005, *ApJL*, **620**, L87
- Waters, C. Z., Magnier, E. A., Price, P. A., et al. 2016, arXiv:1612.05245
- White, C. J., Kasliwal, M. M., Nugent, P. E., et al. 2015, *ApJ*, **799**, 52
- Yaron, O., & Gal-Yam, A. 2012, *PASP*, **124**, 668
- Zhang, M., Fuller, J., Schwab, J., & Foley, R. J. 2019, *ApJ*, **872**, 29